

# Fluid-Structure Interaction Techniques for Parachute

Vinod Kumar<sup>1</sup> and Victor Udoewa<sup>2</sup>

<sup>1</sup>*The University of Texas at El Paso*

<sup>2</sup>*American Association for the Advancement of Science Policy Fellow  
USA*

## 1. Introduction

Fluid-Structure Interaction (FSI) is an inescapable feature of the complicated flow physics where strong coupling between fluid dynamics and structural dynamics occurs. One such example is to understand the behavior of parachutes during canopy inflation and decent. Such simulations can substantially reduce the design costs of parachutes by reducing the number of rather expensive experiments/airdrop tests required. Additionally, FSI simulations can augment experimental approaches by providing detailed fluid flow and structural deformation characteristics of the parachute systems under various scenarios. There are however many computational challenges that one faces in performing the high fidelity FSI simulations. Some of these are turbulence modeling, fluid-structure interaction coupling, the convergence of a nonlinear iteration loop, capturing the physical discontinuity in the flow field, efficiently and accurately solving a large set of linear equations on parallel computers, and improving the parallel performance. Here, we present a high fidelity FSI technique that addresses the coupling issues on High Performance Computing (HPC) environments.

## 2. Mathematical formulations

FSI modeling of parachutes requires simultaneously solving the Navier-Stokes equations (a set of highly nonlinear Partial Differential Equations (PDEs)) for fluid dynamics, structural mechanics, and mesh motions. Parachutes are made of membrane type structure (usually nylon clothes) that goes through large deformation as a result of aerodynamic forces. This often causes the FSI simulations to break down because of the convergence issues of nonlinear and linear iterative solvers and large mesh stretching/distortions. It is, therefore, difficult to operate and requires in-depth knowledge of numerical techniques, fundamentals of fluid and structure dynamics, coupling behavior, programming languages and environments on High-Performance Computing (HPC) systems. Preparations required before FSI simulations for the parachute-systems are equally challenging and poses tremendous difficulties for novice users.

### 2.1 Fluid dynamics (FD)

The physics of fluid dynamics is mathematically represented by the Navier-Stokes equations for compressible and incompressible flows. These equations represent conservation of mass

(continuity), momentum, and energy equations. These equations are a set of time dependent non-linear partial differential equations (PDEs).

**Incompressible flow:** The governing equations of incompressible aerodynamic flows are given by the conservation of mass and momentum equations. The energy equation becomes decoupled from mass and momentum, therefore we do not need to simultaneously solve the energy equations for incompressible flow system. Most parachute flow lies in the incompressible flow regime.

Let  $\Omega_t \subset \mathcal{R}^{n_{sd}}$  be the spatial domain with boundary  $\Gamma_t$  at any instant of time  $t \in (0, T)$  where  $n_{sd}$  is the number of spatial dimensions (= 4 for 3D incompressible fluid i.e. pressure and three components of velocity vectors) and  $T$  is the total time of computations. The spatial coordinates and time are denoted by  $\mathbf{x}$  and  $t$ , respectively. The Navier-Stokes equations of incompressible flows are:

$$\nabla \cdot \mathbf{u} = 0 \text{ on } \Omega_t \forall t \in (0, T) \quad (1)$$

$$\rho \left( \frac{\partial \mathbf{u}}{\partial t} + \mathbf{u} \cdot \nabla \mathbf{u} - \mathbf{f} \right) - \nabla \cdot \boldsymbol{\sigma} = \mathbf{0} \text{ on } \Omega_t \forall t \in (0, T) \quad (2)$$

where  $\rho$ ,  $\mathbf{u}$  and  $\mathbf{f}$  are the density (constant for incompressible flows), velocity, and the external force, respectively. With  $\mathbf{I}$  as the identity matrix, the stress tensor is related to the pressure ( $p$ ) and shear stress tensor ( $\boldsymbol{\tau}$ ) by

$$\boldsymbol{\sigma}(p, \mathbf{u}) = -p\mathbf{I} + \boldsymbol{\tau} \text{ on } \Omega_t \forall t \in (0, T) \quad (3)$$

The shear stress ( $\boldsymbol{\tau}$ ) and strain rate tensor ( $\dot{\boldsymbol{\epsilon}}$ ) are related by the following constitutive relations

$$\boldsymbol{\tau} = 2\mu\dot{\boldsymbol{\epsilon}} \quad (4)$$

where the viscosity of the air ( $\mu$ ) is constant (Newtonian flow assumptions). In this case, it can be shown that the strain rate tensor is related to velocity by the following relationship

$$\dot{\boldsymbol{\epsilon}}(\mathbf{u}) = \frac{1}{2} \left( (\nabla \mathbf{u}) + (\nabla \mathbf{u})^T \right) \quad (5)$$

**Compressible flow:** The governing equations of compressible aerothermodynamics flows are given by the conservation of mass, momentum, and energy equations. These equations are written as follows:

Continuity or conservation of mass equation:

$$\frac{\partial \rho}{\partial t} + \nabla \cdot (\rho \mathbf{u}) = 0 \quad (6)$$

Conservation of momentum equations:

$$\frac{\partial (\rho \mathbf{u})}{\partial t} + \nabla \cdot (\rho \mathbf{u} \mathbf{u}) + \nabla p - \nabla \cdot \mathbf{T} = 0 \quad (7)$$

Conservation of energy equation:

$$\frac{\partial (\rho e)}{\partial t} + \nabla \cdot (\rho e \mathbf{u}) + \nabla (p \mathbf{u}) - \nabla \cdot \mathbf{T} \mathbf{u} + \nabla \cdot \mathbf{q} = 0 \quad (8)$$

Above conservative equations (Eqs 6-8) can be simplified and written in advective-diffusive flux terms as follows:

$$\frac{\partial \mathbf{U}}{\partial t} + \frac{\partial \mathbf{F}_i}{\partial x_i} - \frac{\partial \mathbf{E}_i}{\partial x_i} = \mathbf{0} \quad (9)$$

where  $\mathbf{U}$  is a vector containing the primitive variables and is given as

$$\mathbf{U} = (\rho, \rho u_1, \dots, \rho u_{n_{sd}}, \rho e)^T \quad (10)$$

where  $\rho$  is density,  $u_i$  is the velocities, and  $e$  is the total energy per unit mass. The subscript denotes space dimension (i.e., 1 for x-direction, 2 for y-direction and 3 for z-direction, e.g.,  $u_1$  is x-component of the velocity) and  $n_{sd}$  stands for number of space dimension (i.e.,  $n_{sd} = 1$  for 1-D problem,  $n_{sd} = 2$  for 2-D problem and  $n_{sd} = 3$  for 3-D problem. Here, the Euler flux  $\mathbf{F}_i$  is given by

$$\mathbf{F}_i = (u_i \rho, u_i \rho u_1 + \delta_{i1} p, \dots, u_i \rho u_{n_{sd}} + \delta_{i n_{sd}} p, u_i (\rho e + p))^T \quad (11)$$

where  $\mathbf{E}_i$  is viscous flux and is given by

$$\mathbf{E}_i = (0, \tau_{i1} \rho, \dots, \tau_{i n_{sd}}, -q_i + \tau_{ik} u_k)^T \quad (12)$$

Here,  $p$  is the mechanical pressure and  $\tau_{ij}$  is the viscous stress tensor. Eq (9) is further simplified and written in Euler-Jacobian advective and diffusive matrices form as

$$\frac{\partial \mathbf{U}}{\partial t} + \mathbf{A}_i \frac{\partial \mathbf{U}}{\partial x_i} - \frac{\partial}{\partial x_i} \left( \mathbf{K}_{ij} \frac{\partial \mathbf{U}}{\partial x_j} \right) = \mathbf{0} \quad (13)$$

where Euler-Jacobian advective matrix,  $\mathbf{A}_i$ , is given by

$$\mathbf{A}_i = \frac{\partial \mathbf{F}_i}{\partial \mathbf{U}} \quad (14)$$

and the diffusive matrix,  $\mathbf{K}_{ij}$ , is given by

$$\mathbf{K}_{ij} \frac{\partial \mathbf{U}}{\partial x_j} = \mathbf{E}_i \quad (15)$$

The advective and diffusive coefficients are not constant and often strongly depend on the local Mach number of the flows, speed of sound, and viscous dissipation and hence are strongly dependent on the solution itself. The coefficients are derived in (Le Beau & Tezduyar, 1991; Kumar, 2005).

The advective and diffusive coefficients are not constant and often strongly depend on the local Mach number of the flows, speed of sound, and viscous dissipation and hence are strongly dependent on the solution itself. The coefficients are derived in (Le Beau & Tezduyar, 1991; Kumar, 2005).

## 2.2 Structural dynamics (SD)

The deformation of the flexible parachute structure is governed by the equations of large deformation in the structure mechanics under the influence of external driving force arising from dynamic fluid pressure and shear stresses loading from FD. The governing equations for structural dynamics are obtained from the conservation of linear momentum and are given by:

$$\rho^s \left( \frac{d^2 \mathbf{y}}{dt^2} + \eta \frac{d\mathbf{y}}{dt} - \mathbf{f}^s \right) - \nabla \cdot \boldsymbol{\sigma}^s = \mathbf{0} \quad (16)$$

where  $\rho^s$  is the material density,  $\mathbf{y}$  is the displacement vector,  $\mathbf{f}^s$  is the external force body forces,  $\boldsymbol{\sigma}^s$  is the Cauchy stress tensor, and  $\eta$  is the mass proportional damping coefficient. The mass-proportional damping provides additional stability, but can significantly affect the dynamics of the structure. Here, we assume large displacements and rotations, but small strains for nonlinear analysis. The second Piola-Kirchhoff stress (force per unit area in the original configuration) tensor,  $\mathbf{S}$ , and the Green-Lagrange strain (in the original configuration) tensor,  $\mathbf{E}$ , are used to write the constitutive equations using the total Lagrangian formulation. Thus, stresses are expressed in terms of the 2nd Piola-Kirchhoff stress tensor. The 2nd Piola-Kirchhoff stress tensor is related to Cauchy stress (force per unit area in deformed configuration) tensor,  $\boldsymbol{\sigma}^s$ , by the kinematic transformation,  $\mathbf{s} = \frac{\rho_0}{\rho^s} \mathbf{F} \boldsymbol{\sigma}^s \mathbf{F}^T$  where  $\rho_0$  is the density in the original configuration and  $\mathbf{F}$  ( $=\mathbf{g}\mathbf{G}$ ;  $\mathbf{g}$ =covariant tensor in deformed configuration,  $\mathbf{G}$ =contravariant tensor in original configuration). Firstly, we will assume linear stress-strain relations (Hookean materials) and plane stress conditions. The constitutive equations are given by

$$S^{ij} = \{\bar{\lambda} G^{ij} G^{jk} + \mu (G^{il} G^{jk} + G^{ik} G^{jl})\} E_{kl} \quad (17)$$

where  $\bar{\lambda} = \frac{2\lambda\mu}{\lambda+2\mu}$  ( $\lambda$  &  $\mu$  are the Lamé constants). The Lamé constants are related to the Young's modulus  $Y$  and the Poisson's  $\nu$  ratio by:  $\bar{\lambda} = \frac{\nu Y}{(1+\nu)(1-2\nu)}$  and  $\mu = \frac{Y}{2(1+\nu)}$ . Dirichlet- and Neumann-type BCs are  $\mathbf{y}=\mathbf{g}^s$  and  $\mathbf{n} \cdot \boldsymbol{\sigma}^s=\mathbf{t}^s$  where  $\mathbf{g}^s$  is the specified displacements and  $\mathbf{t}^s$  is traction forces (shear stress from the fluid dynamics). The initial conditions are  $\mathbf{y} = \mathbf{0}$  &  $\frac{d\mathbf{y}}{dt} = \mathbf{0}$ .

### 2.3 Mesh deformation (MD)

Fluid mesh is considered as elastic materials which deforms along with SD deformation. The governing equations mesh deformation is given by

$$\nabla \cdot \boldsymbol{\sigma}^M = 0 \quad (18)$$

## 3. Finite element discretization

The finite element method is a numerical tool for obtaining solutions to boundary value engineering problems governed by partial differential equations as described in the previous section. It is especially attractive for problems that involve complex geometries where other numerical methods, such as spectral or finite difference methods, are difficult to apply. The principle of the method is to replace an entire continuous domain by a number of sub-domains in which the unknown function is represented by simple interpolation functions with unknown coefficients. Thus, the original boundary-value problem with an infinite number of degrees of freedom is converted into a problem with a finite number of degrees of freedom or, in other words, the solution of the whole system is approximated by a finite number of unknown coefficients. Here, we construct a discretization of a weighted residual formulation in order to arrive at a linear matrix equation. The discretization can be applied in space and time. This formulation is called the space-time finite element method. Alternatively, one can carry out the discretization in space only. Such a method is called a semi-discrete formulation. Details of these methods can be found in a number of references (Tezduyar, Behr, & Liou, 1992; Shakib, 1988; Behr & Tezduyar, 1994).

Galerkin approximation methods are used for the finite element formulations. Galerkin methods are among the most commonly used weighted residual methods. In structural analysis, where often the minimization of energy is the underlying idea, the application of Galerkin methods leads to symmetric matrices and provides *optimal* results. By *optimal* we mean that the solution possesses the best approximation property. The difference between the approximate and the exact solutions is minimized with respect to a certain norm as shown by (Brooks & Hughes, 1982).

The situation, however, is very different in the presence of advective terms. The matrix associated with the advective term is non-symmetric and the best approximation property is lost (Brooks & Hughes, 1982). As a result Galerkin methods applied to these problems are far from optimal and show spurious node-to-node oscillations in the solutions, worsening with growing advection-domination. This not only leads to qualitatively incorrect results but also violates basic physical principles like the second law of thermodynamics (Hirsch, 1988). The pollution of the solution with oscillations is dependent on the domination of the advection terms over other terms of the differential equation. Domination of advection is determined by dimensionless numbers such as Reynolds (ratio of inertial to viscous terms) or Peclet (ratio of advection to diffusion terms). The larger these numbers are, the more dominant is the advection term and the stronger is the numerical node-to-node oscillations in the results. Brooks and Hughes (Brooks & Hughes, 1982) introduced the Streamline-Upwind/Petrov-Galerkin (SUPG) method and this method can be considered as the first successful stabilization technique to prevent oscillations in advection-dominated problems. The SUPG method introduces artificial diffusion in the streamline direction. The introduction of artificial diffusion is done in a consistent way. This can be interpreted as a modification of the test function in the advection direction. Therefore, the weak (variational) form still satisfies the exact solution of the problem.

Another source of potential instabilities in standard Galerkin methods arises when velocity and pressure interpolation functions are not chosen from compatible spaces. Babuska and Brezzi (Babuska, 1973; Brezzi, 1974) showed that compatible spaces must satisfy the *inf-sup* conditions. If they are not chosen from compatible spaces, then oscillatory behavior is observed, primarily in the pressure field. Unfortunately, much desirable function spaces are precluded due to Babuska-Brezzi conditions. Most computationally attractive combinations are the ones which employ equal order interpolations. Hughes et al. proposed a consistent way to circumvent the *inf-sup* condition for the Stokes problem (Hughes, Franca, & Mallet, 1986). As a generalization, Tezduyar, et al., proposed a Pressure-Stabilized/Petrov-Galerkin (PSPG) formulation for finite Reynolds number flows (Tezduyar, Mittal, Ray, & Shih, 1992). The PSPG formulations reduces to the one proposed by Hughes et al. formulation in the limiting case when the Reynolds number tends to zero.

### 3.1 Deforming spatial domain/stabilized space-time (DSD/SST) formulations for incompressible flows

In order to construct the finite element function spaces for the space-time method, the time interval  $(0, T)$  is partitioned into sub-intervals  $I_n = (t_n, t_{n+1})$ , where  $t_n$  and  $t_{n+1}$  belong to an ordered sequence of time levels  $0 = t_0 < t_1 < \dots < t_N = T$ . Let  $\Omega_n = \Omega_{t_n}$  and  $\Gamma_n = \Gamma_{t_n}$ . The space-time slab  $Q_n$  is defined as the domain enclosed by the surfaces  $\Omega_n$ ,  $\Omega_{n+1}$ , and  $P_n$ , where  $P_n$  is the surface described by the boundary  $\Gamma_t$  as  $t$  traverses  $I_n$ . As is the

case with  $\Gamma_t$ , surface  $P_n$  can be decomposed into  $(P_n)_g$  and  $(P_n)_h$  with respect to the type of boundary condition (Dirichlet or Neumann) being applied for a degree of freedom of unknown vector  $\mathbf{d}$ .

A space-time slab for a 2D spatial domain is schematically shown in Figure 1. The volume of the slab is the volume traversed by the two dimensional plane in time and is given by  $Q_n$ . The boundary is denoted by  $P_n$ . For a three spatial dimension problem, one can visualize this as a four dimensional space. The spatial domain at  $t = t_n$  denoted by  $\Omega_n$  and at  $t = t_{n+1}$  by  $\Omega_{n+1}$ . In the beginning of the computations at  $t = 0$ , the spatial domain and its boundary is denoted by  $\Omega_0$  and  $\Gamma_0$  respectively. Defining spatial domain in this way allows one to handle moving and deforming bodies.

For each space-time slab, we define the following finite element interpolation function spaces for the conservation variables

$$(\mathcal{S}_u^h)_n = \{u^h | u^h \in [H^{1h}(Q_n)^{n_{sd}}], u^h \cong g_u^h \text{ on } (P_n)_g, d = 1, \dots, n_{sd}\} \tag{19}$$

$$(\mathcal{V}_u^h)_n = \{w^h | w^h \in [H^{1h}(Q_n)^{n_{sd}}], w^h \cong 0 \text{ on } (P_n)_g, d = 1, \dots, n_{sd}\} \tag{20}$$

$$(\mathcal{S}_p^h)_n = (\mathcal{V}_p^h)_n = \{q^h | q^h \in [H^{1h}(Q_n)^{n_{sd}}], w^h \cong 0 \text{ on } (P_n)_g\} \tag{21}$$

where  $H^{1h}(Q_n)$  is the finite-dimensional function space over the space-time slab  $Q_n$ . Over the element domain, this space is formed by using first-order polynomials in both space and time. The interpolation functions are continuous in space but discontinuous in time. The stabilized space-time (SST) formulation of momentum balance and continuity equations for deforming spatial domains (DSD) can be written as follows.

Given  $(u^h)_n^-$ , find  $u^h \in (\mathcal{S}_u^h)_n$  and  $p^h \in (\mathcal{S}_p^h)_n$  such that  $\forall w^h \in (\mathcal{V}_u^h)_n$  and  $q^h \in (\mathcal{V}_p^h)_n$

$$\begin{aligned} & \int_{Q_n} \mathbf{w}^h \cdot \rho \left( \frac{\partial \mathbf{u}^h}{\partial t} + \mathbf{u}^h \cdot \nabla \mathbf{u}^h + \mathbf{f}^h \right) dQ + \int_{Q_n} \dot{\boldsymbol{\varepsilon}}(\mathbf{w}^h) : \boldsymbol{\sigma}(p^h, u^h) dQ + \int_{\Omega_n} q^h \nabla \cdot \mathbf{u}^h dQ + \\ & + \sum_{e=1}^{(n_{el})_n} \int_{Q_e^c} \tau \left[ \rho \left( \frac{\partial \mathbf{w}^h}{\partial t} + \mathbf{u}^h \cdot \nabla \mathbf{w}^h + \mathbf{f}^h \right) - \nabla \cdot \boldsymbol{\sigma}(q^h, w^h) \right] \cdot \left[ \rho \left( \frac{\partial \mathbf{u}^h}{\partial t} + \mathbf{u}^h \cdot \nabla \mathbf{u}^h + \mathbf{f}^h \right) - \nabla \cdot \boldsymbol{\sigma}(p^h, u^h) \right] dQ + \tag{22} \\ & + \sum_{e=1}^{(n_{el})_n} \int_{Q_e^c} \delta \nabla \cdot \mathbf{w}^h \rho \nabla \cdot \mathbf{u}^h dQ + \int_{\Omega_n} (\mathbf{w}^h)_n^+ \cdot \rho \left( (\mathbf{u}^h)_n^+ + (\mathbf{u}^h)_n^- \right) d\Omega = \int_{(P_n)_h} \mathbf{w}^h \cdot \mathbf{h}^h dP \end{aligned}$$

This process is applied sequentially to all the space-time slabs  $Q_1, Q_2, \dots, Q_{N-1}$ . At the start of the computations, we assume  $(u)_0^+ = u_0$ . In the equation (22), the first three terms, the sixth term, and the right-hand-side comprise the Galerkin formulation of the problem. The first element-level integrals (terms under the summation  $\sum_{e=1}^{(n_{el})_n}$ ) in equation are least-squares terms based on the momentum equation. The second element-level integrals are added to the formulation for numerical stability at high Reynolds numbers. These least-squares terms are based on the continuity equation. The stabilization coefficients,  $\tau$  and  $\delta$ , are defined at the element level. Both stabilization terms are weighted residuals, and therefore maintain the consistency of the formulation. Since the interpolation functions are discontinuous in time, the sixth term weakly enforces continuity of the velocity field across the space-time slabs.

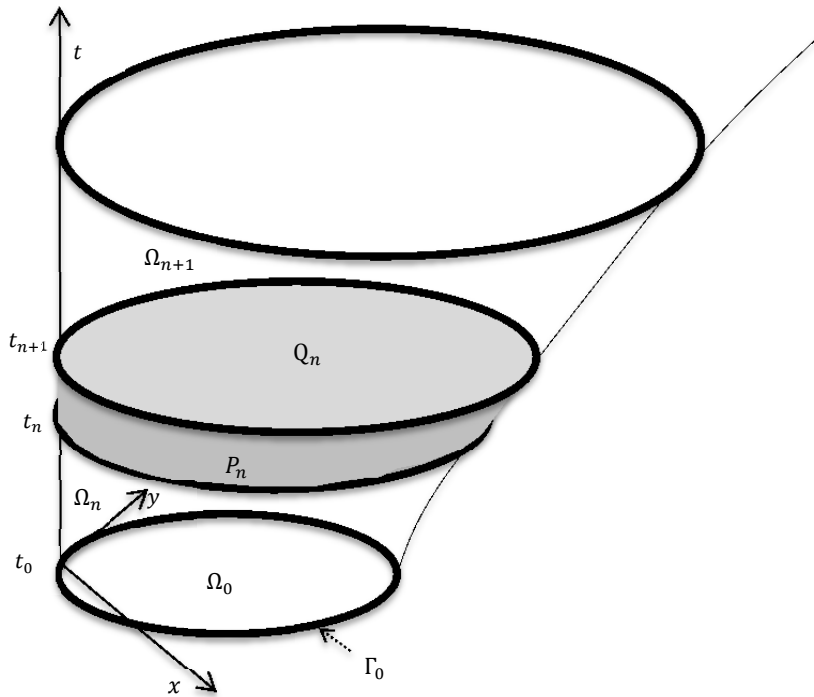


Fig. 1. Space time slab for deforming spatial domain

The stabilization coefficients,  $\tau$  and  $\delta$ , are given by

$$\tau = \left[ \left( \frac{z}{\Delta t} \right)^2 + \left( \frac{2|u^h|}{h_e} \right)^2 + \left( \frac{4\nu}{h_e^2} \right)^2 \right]^{-\frac{1}{2}} \tag{23}$$

$$\delta = \frac{h_e}{z} |u^h| \tag{24}$$

where  $\nu$  is the kinematic viscosity,  $\Delta t$  is the time step, and  $h_e$  is a suitable measure of element length. One obvious choice for element length is the maximum edge length. This, however, gives rise to excessive numerical diffusion when the flow direction is not aligned along the maximum edge. A directional element length based on advection direction works better in this case. The parameter  $z$  is defined as

$$z = \begin{cases} \left( \frac{Re_u}{3} \right) & \text{if } Re_u \leq 3 \\ 1 & \text{if } Re_u > 3 \end{cases} \tag{25}$$

where  $Re_u = \frac{|u^h| h_e}{2\nu}$  is the element Reynolds number.

The DSD/SST formulation compressible equations are written in the similar fashion. A detailed discussion of these stabilization terms and their origin can be found in (Mittal, 1992).

## 4. Coupling techniques

### 4.1 Multiphysics coupling techniques

Let us symbolically write the nonlinear system of equations arising from finite element discretization for the partial differential equations (PDEs) of a three physical systems, for example, *Physics 1*, *Physics 2*, and *Physics 3*, as a nonlinear set of equations denoted by scalar functions

$$\mathbf{N}_1(\mathbf{d}_1, \mathbf{d}_2, \mathbf{d}_3) = 0 \quad (26)$$

$$\mathbf{N}_2(\mathbf{d}_1, \mathbf{d}_2, \mathbf{d}_3) = 0 \quad (27)$$

$$\mathbf{N}_3(\mathbf{d}_1, \mathbf{d}_2, \mathbf{d}_3) = 0 \quad (28)$$

where the subscript "1", "2", and "3" represent *Physics 1*, *Physics 2*, and *Physics 3* respectively (e.g., SD, MD, and FD) for our case. This representation can be extended to cases with more than three multiphysics processes. Here,  $\mathbf{d}_1$ ,  $\mathbf{d}_2$ , and  $\mathbf{d}_3$  are the vectors of unknown variables for *physics 1* (e.g., deformed coordinate systems and velocity), *physics 2* (e.g., deformed mesh coordinate systems), and *physics 3* (e.g., velocity, pressure, and density for FD). The coupling among different physics arises from boundary conditions at the interfaces of various systems.

Linearization of the nonlinear set of equations through first order Newton-Raphson iterative approximation results in

$$\left[\frac{\partial \mathbf{N}_1}{\partial \mathbf{d}_1}\right]^i \Delta \mathbf{d}_1^{i+1} + \left[\frac{\partial \mathbf{N}_1}{\partial \mathbf{d}_2}\right]^i \Delta \mathbf{d}_2^{i+1} + \left[\frac{\partial \mathbf{N}_1}{\partial \mathbf{d}_3}\right]^i \Delta \mathbf{d}_3^{i+1} = -[\mathbf{N}_1(\mathbf{d}_1, \mathbf{d}_2, \mathbf{d}_3)]^i \quad (29)$$

$$\left[\frac{\partial \mathbf{N}_2}{\partial \mathbf{d}_1}\right]^i \Delta \mathbf{d}_1^{i+1} + \left[\frac{\partial \mathbf{N}_2}{\partial \mathbf{d}_2}\right]^i \Delta \mathbf{d}_2^{i+1} + \left[\frac{\partial \mathbf{N}_2}{\partial \mathbf{d}_3}\right]^i \Delta \mathbf{d}_3^{i+1} = -[\mathbf{N}_2(\mathbf{d}_1, \mathbf{d}_2, \mathbf{d}_3)]^i \quad (30)$$

$$\left[\frac{\partial \mathbf{N}_3}{\partial \mathbf{d}_1}\right]^i \Delta \mathbf{d}_1^{i+1} + \left[\frac{\partial \mathbf{N}_3}{\partial \mathbf{d}_2}\right]^i \Delta \mathbf{d}_2^{i+1} + \left[\frac{\partial \mathbf{N}_3}{\partial \mathbf{d}_3}\right]^i \Delta \mathbf{d}_3^{i+1} = -[\mathbf{N}_3(\mathbf{d}_1, \mathbf{d}_2, \mathbf{d}_3)]^i \quad (31)$$

where superscript  $i$  is the nonlinear iteration counter for the coupled systems. This linearized system of equations can be written in simplified matrix notation as

$$\begin{bmatrix} \mathbf{A}_{11} & \mathbf{A}_{12} & \mathbf{A}_{13} \\ \mathbf{A}_{21} & \mathbf{A}_{22} & \mathbf{A}_{23} \\ \mathbf{A}_{31} & \mathbf{A}_{32} & \mathbf{A}_{33} \end{bmatrix}^i \begin{bmatrix} \Delta \mathbf{d}_1 \\ \Delta \mathbf{d}_2 \\ \Delta \mathbf{d}_3 \end{bmatrix}^{i+1} = \begin{bmatrix} \mathbf{b}_1 \\ \mathbf{b}_2 \\ \mathbf{b}_3 \end{bmatrix}^i \quad (32)$$

where the Jacobians of the iterative solver are given by

$$\mathbf{A}_{jk} = \frac{\partial \mathbf{N}_j}{\partial \mathbf{d}_k} \quad (33)$$

and the right hand side vector is given by

$$\mathbf{b}_j = -[\mathbf{N}_j(\mathbf{d}_1, \mathbf{d}_2, \mathbf{d}_3)] \quad (34)$$

These systems of equations represent a fully coupled multiphysics (three physics in this case) system. For most real life applications, the cross-Jacobians terms (e.g.,  $\mathbf{A}_{12}$  &  $\mathbf{A}_{13}$ ) that represents the coupling process (e.g., the instantaneous feedback that the structure gets from

the fluid flow for any small deformation in the structure) and are usually mathematically not well defined by partial differential equations.

Most commercial/opensource software treat fully coupled system through nonlinear iterations but assume one directional coupling inside the nonlinear iterations. This results in a diagonal Jacobian matrices (symbolizing one way coupling) and can be written by setting off diagonal terms equal to zeros as

$$\begin{bmatrix} \mathbf{A}_{11} & \mathbf{0} & \mathbf{0} \\ \mathbf{A}_{21} & \mathbf{A}_{22} & \mathbf{0} \\ \mathbf{A}_{31} & \mathbf{A}_{32} & \mathbf{A}_{33} \end{bmatrix}^i \begin{bmatrix} \Delta \mathbf{d}_1 \\ \Delta \mathbf{d}_2 \\ \Delta \mathbf{d}_3 \end{bmatrix}^{i+1} = \begin{bmatrix} \mathbf{b}_1 \\ \mathbf{b}_2 \\ \mathbf{b}_3 \end{bmatrix}^i \quad (35)$$

In case of FSI modeling, this implies that SD (*Physics 1*) is solved first using a forcing terms (shear and pressure coming out from FD i.e., *Physics 3*), then MD (*Physics 2*) is solved using deformed coordinate systems at the structure boundaries of the FD systems, and at the end FD (*Physics 3*) is solved using the deformed mesh from MD and velocity boundary conditions at the interfaces. In this, the coupling terms ( $\mathbf{A}_{21}$ ,  $\mathbf{A}_{31}$ , and  $\mathbf{A}_{32}$ ) are computed through Least-Square projections for incompatible meshes or mapping for compatible meshes.

One way coupling however fails if the coupling between structure and fluid is strong such parachute - aerodynamics systems. Other challenges are addressing the multiscale nature of such problems (e.g., temporal and spatial scales of structure dynamics usually occur at a lot smaller scales than the fluid dynamics). New advancement in computational technologies such multi-grid preconditioning for multi-physics/multi-scale advance linear solver on massively parallel computers come help address some of these challenges. Numerical convergence of the system can also be enhanced by advanced solvers. Discussions about these are beyond the scope of this chapter.

## 4.2 FSI coupling techniques for parachutes

As described in the previous sections, the FSI modeling of parachute involves solving the time dependent fluid dynamics (FD) equations together with structural dynamics (SD) and mesh deformation (MD) equations as described in the previous section. Coupling between structure and fluid is achieved by exchange of information (i.e., pressure  $p$ , velocity  $v$ , surface coordinates, and temperature) from the aerodynamics simulations to Interface (through mapping) and from the Interface to structural dynamics. We employ least-square projections if the meshes between two segments are incompatible. Here, we assume that the interface has the same mesh morphology as the fluid dynamics (FD) mesh on the object surface but it differs from the SD meshes (usually requires higher order finite element meshes to resolve the surface deformations). Fluid dynamics is governed by 3D gas dynamics equations and structural dynamics is modeled as 3D constitutive equations for solid mechanics. Coupling is achieved in block iterative fashion as shown in the figure 6. In block iterative method, first SD is solved using finite element methods for solid mechanics. Then, new mesh coordinates are determined by solving the elastodynamics equations for mesh deformation. Note that fluid meshes have no physical physics, so Young's modulus of the mesh elements is adjusted in such way those mesh-motion results in minimal element distortions. After mesh motion, FD is solved using the new coordinates in the fluid domain and velocity boundary conditions and the surface.

The whole process is repeated inside a non-linear Newton-Raphson iterations block (as shown in Figure 2) until a desired convergence or maximum number of iterations (set by user) is achieved.

For compressible flow, we compute pressure using the ideal gas conditions for air from the conservative (primitive) variables (i.e.,  $\rho, \rho \mathbf{u}, \rho e$ ) which are computed by solving fluid dynamics equations.

$$p = \rho R \theta = (\gamma - 1) \rho i = (\gamma - 1) \left[ \rho e - \frac{|\rho \mathbf{u}|^2}{2\rho} \right] \quad (36)$$

where  $R$  is the ideal gas constant,  $i$  is the internal energy,  $\theta$  is the temperature, and is the ratio of specific heat (usually = 1.4 for mono atomic gases). The boundary conditions for uid velocity on the structure interface boundaries are given by

$$[U_1, U_2, U_3] = [\rho u_1, \rho u_2, \rho u_3]_{interface} \quad (37)$$

### 4.3 Mesh generation and update

Proper selection of the appropriate mesh update approach depends on several factors. These include the complexity of the moving boundary (or interface) as well as the overall geometry, the unsteadiness of the moving boundary (or interface), and the qualities of the starting mesh. In general, the mesh update should have two components: moving the mesh for as long as it is possible, and full or partial remeshing (i.e. generating a new set of elements, and sometimes also a new set of nodes) when element distortion becomes too high.

In mesh moving strategies, our only requirement for the mesh motion is that at the moving boundary (or interface) the normal velocity of the mesh has to match the normal velocity of the uid. Beyond that, the mesh can be moved in any way desired, with the main objective being to reduce the frequency of remeshing. In 3D simulations that rely on an automatic mesh generator, the cost of automatic mesh generation becomes a major reason for trying to reduce the frequency of remeshing. Additionally, mesh generation is often done on a single CPU, losing the parallel performance. Furthermore, when we remesh we need to project the solution from the old mesh onto the new one. This step introduces projection errors along with an additional computational cost that is not trivial for 3D computations involving complex geometries. Projection errors can destroy the divergence free condition in the domain giving rise to pressure oscillations (Udoewa, 2005). All of these factors provide a strong motivation for utilizing mesh update strategies which minimize the frequency of remeshing.

Parachute simulations involve complex geometries and arbitrary motions for which it is difficult to design special purpose mesh moving techniques. For parachute clusters, the behavior of parachute interactions becomes even more erratic. For these problems I use an automatic mesh moving scheme (Johnson A. , 1995; Stein, Simulation and Modeling Techniques for Parachute Fluid-Structure Interactions, 1999; Udoewa, 2005) to move the nodal points, as governed by the equation of linear elasticity, and where the smaller elements enjoy more protection from mesh deformation. The motion of the internal nodes is determined by solving these additional equations. The boundary conditions for the mesh motion are specified in such a way that they ensure the matching of the normal velocity of the fluid at the interface.

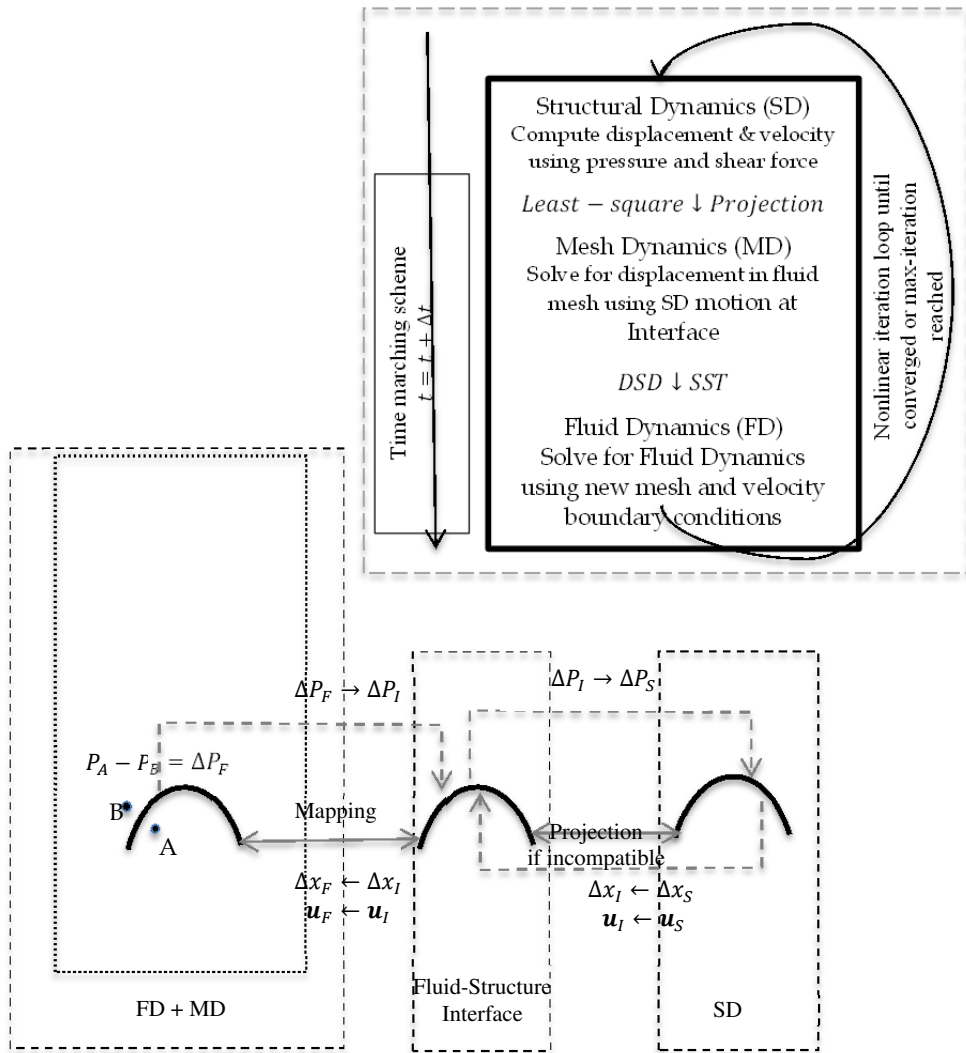


Fig. 2. Block iterative coupling technique (top-right) and information exchange processes to address the coupled multiphysics problems

#### 4.4 Incompatible meshes

Incompatible meshes [40] for structure and interface surface are used. This allows one to choose different types (e.g. higher order bi-quadratic elements for parachute canopy and triangular mesh for fluid-structure interface) and different refinements. For parachute discretization, we choose the same type of triangular elements for both parachute canopy

and fluid-structure interface meshes but the canopy mesh for the structural dynamics was very refined to resolve the spatial scales of the gores of the canopy. The same level of mesh refinement for the fluid-structure interface mesh (in case compatible case) was not suitable due to resulting large number elements of the fluid meshes and computationally expensive Navier-Stokes equation solver. Additionally, the length scale associated with fluid dynamics process is smaller than the scale required for structural dynamics to achieve the same level of fidelity. Level of refinement of the meshes were decided based on extensive parachute modeling experiences and should be decided on case-by-case basis. This resulted in incompatible meshes and consequently a mechanism to transfer the deformed coordinate and velocity information from SD to FD and pressure and shear stresses from FD to SD.

Whether one uses different types of elements or different levels of refinements, a projection mechanism is needed to transfer the information from fluid to structure and vice-versa. Errors (usually called projection errors) come along with the projection. Some of the projection techniques are the linear projection and the least-square projection. We used the least-square projection technique to achieve this goal. The least-square projection technique minimizes the sum of residuals in the entire domain. The least-square projection is achieved by solving the following minimization problem

$$\min \int_{\Gamma^I} |\mathbf{d}_S - \mathbf{d}_F|^2 d\Gamma \quad (38)$$

where  $\mathbf{d}_F$  (the fluid variables, e.g., pressure drop across the canopy) is projected to  $\mathbf{d}_S$  (the structure variables, e.g., pressure applied on the canopies). Integration is carried over the interface domain  $\Gamma^I$ . Similar techniques are used to project the velocity and displacement from structure to the fluid-interface.

#### 4.5 Pressure ramping

For some cases, the ramping of pressure was absolutely necessary to obtain converged solutions. It was desirable especially in those cases where the guess for the initial shape of the parachute canopies was not close to the real life parachute geometry. The convergence of nonlinear interactions at the start of the FSI simulations was very erratic in the absence of a ramping technique. Pressure ramping was successfully used in these cases. Here, the information exchange between structure and fluid is linearly ramped. The ramping is carried out such that the acting pressure on the canopy is equal to the guess pressure (used for inflating the parachute) at the start of the FSI simulations and equal to the fluid pressure at the end of the ramping. This is achieved by

$$\Delta P_S \leftarrow r(t)\Delta P_G + (1 - r(t))\Delta P_F \quad (39)$$

where  $\Delta P_S$  is the effective pressure applied on the structure,  $\Delta P_G$  is the guess pressure used to get the inflated shape of the parachute, and  $\Delta P_F$  is the pressure drop across the canopies coming from fluid simulations. The ramping factor  $r(t)$  is assumed to be linear in time and varies from 0 to 1 in time  $t_{ramp}$  where  $t_{ramp}$  is the ramping time. Ramping time were chosen case-by-case to achieve appropriate convergence of the Newton-Raphson iterations for the coupled non-linear FSI system.

## 5. FSI Simulations of parachutes

The parachute canopy is made of very flexible fabric materials. It responds quickly to any small changes in fluid behavior. Consequently, there is a strong interaction between the fluid and structure. Bigger the canopies, stronger will be the interactions. Stronger interactions make the problem very nonlinear in nature and hence increase the difficulty of numerical modeling.

### 5.1 Cluster of two G-12 parachutes

A single G-12 parachute is used to drop cargo weighing up to 2,200 lb. There is an interest in the Army for parachute systems that can drop cargos exceeding 2,200 lb. In order to achieve this objective, multiple parachutes in cluster configurations are often used.

The opening stage of a parachute to a fully inflated shape is a critical issue. Usually more than one stage is used to get the fully inflated shape of parachutes in a cluster configuration. One example of multi-stage opening is the use of drogue parachutes. First, a drogue parachute opens and then it pulls the other two G-12 parachutes. After all the parachutes are fully opened, the challenge is to safely drop the cargo into the hands of the right people. The strong parachute-to-parachute aerodynamic interaction can potentially destroy the efficiency of the system if it is not carefully designed. Various researchers have analyzed the cluster of parachute systems using both drop tests and computer simulations. Butler (Butler, 2001) presented the qualitative results from the airdrop tests using a drogue parachute to deploy the G-12 canopies. From the snapshots of a cluster of three G-12 canopy airdrop tests, one clearly observes strong interactions between fluid and canopies. Sahu, et al., (Sahu & Benney, 1997) carried out the numerical simulations using a quasi-static approach by imposing a symmetry condition for the three canopies in an attempt to predict the equilibrium configuration of a cluster of three half-scaled C-9 parachutes. Stein et al. presented results from the semi-discrete simulations for the aerodynamic interactions between the canopies of parachute clusters of varying numbers and arrangements. In these computations, the canopies were assumed to be rigid. In real life, however, the canopy of a parachute deforms in accordance with aerodynamic forces. The placement of parachutes in cluster configuration does not remain stationary. Therefore, FSI simulations are needed to replicate the real life scenario and to understand the dynamics of cluster of parachutes. Here, we present results from the FSI simulations of a cluster of two G-12 parachutes. The results from a cluster of three G-12 parachutes will be discussed in the next section. The DSD/SST formulations as discussed in the section 0, along with appropriate mesh-update strategies, allowed me to study the interaction of canopies in a cluster.

#### **Problem setup:**

The G-12 is a 64 ft diameter cargo parachute designed to deliver a payload of 2200 lb at a descent speed of approximately 28 ft/s. Clusters of G-12 parachutes are commonly used to deliver larger payloads. The G-12 is constructed with 64 suspension lines which extend to risers. For a single G-12 parachute, the confluence point of the risers is connected to a retraction cable which supports the payload. For a cluster of two G-12 parachutes, the retraction cable is connected to two cables, which connect to the confluence point of the risers for the two G-12 parachutes.

The structural model is composed of membranes, cables, and concentrated masses. The canopy is modeled with triangular membrane elements. Linear cable elements are used to model the suspension lines, radial reinforcements along the canopy, risers, and payload support cables. In each example, the payload is modeled with a single concentrated mass. Material properties are selected to be representative of the G-12. A model for the cluster of G-12 parachutes in constructed (unstressed) and inflated (prestressed) configurations is shown in Figure 3.

Several preparations are required for each fluid-structure interaction simulation. First, a stand-alone structural deformation simulation is carried out to determine the inflated (i.e. prestressed) shape of the G-12. The initial inflation pressure is assumed to be equal to stagnation pressure. From my experience, we observed that this pressure gives a better approximation for the initial shape of the parachute canopies. The prestressed configuration for the G-12 cluster is shown in Figure 3 (right). The unstressed configuration is shown in Figure 3 (left).

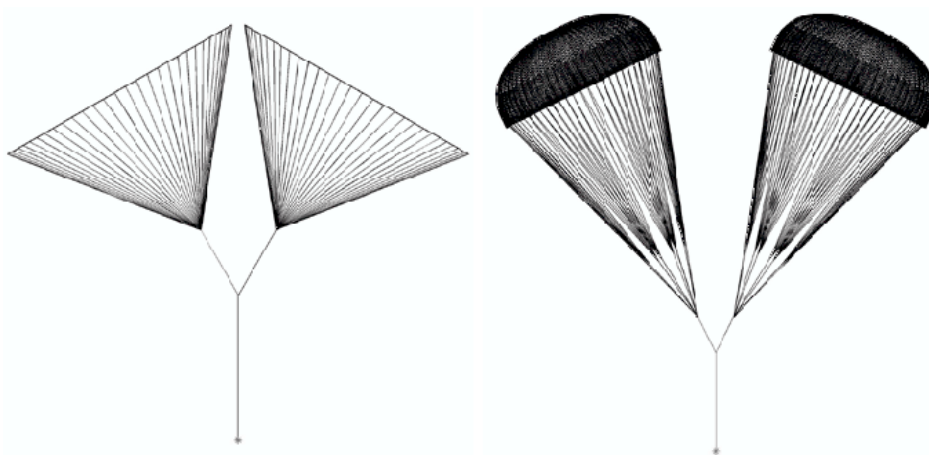


Fig. 3. Cluster of two G-12 parachutes: Constructed (left) and prestressed (right) structural model.

Using the parachute canopy from the prestressed configuration, a fluid mesh is generated and a stand-alone fluid simulation is carried out to obtain a developed flow. Fluid simulations are expensive and time consuming. Therefore, to arrive at developed flow quickly, at first semi-discrete (Johnson A. , 1995; Mittal, 1992) formulation is used to compute the flow field. Semi-discrete formulations are first order in time. Using this solution as the initial condition, space-time (Tezduyar T. E., Stabilized finite element formulations for incompressible flow computations, 1992) computations are carried out. We

start the simulations with a first order-time accurate integration scheme. This helps to clear the start-up vortices quickly. Startup vortices are generated due to large differences in the initial conditions and the exact solutions. After the start-up vortices are cleared from the domain, the second order accurate time-integration scheme is applied. Now, the stage is set to start fluid-structure interaction simulations. Using the results from space-time simulations, a fluid-structure interaction computation is carried out. To remove the mismatch in the initial guessed prestressed configuration, we use the pressure ramping to soften the exchange of information.

### **Pinned payload:**

The pinned payload case corresponds to the wind tunnel testing where parachutes are fixed to a confluence point. The payload is pinned and is not allowed to move in any direction. The objective here is to understand the aerodynamics of two G-12 flexible canopies. Figure 4 presents the parachute cluster showing the deformed shapes and canopy pressure at different instances of time. Color coding ranging from blue to red represents low to high magnitudes of pressure, respectively. At the time  $t = 00:27s$ , two parachute canopies are close to each other. They move away from each other as time progresses. This may be because the initial configuration that I assumed to start the FSI simulations is not in equilibrium. The canopies become after ( $t = 03:36s$ ) as a result of change in pressure distribution. One notices a strong interaction between the uid and the canopies. Pressure distribution keeps changing with time. Parachute canopies are made of very flexible fabric materials and modeled as a membrane structure in the FSI simulations. As a result, the canopies quickly respond to any change in pressure distribution by adjusting their shape as observed in Figure 4. As a result of dynamic behavior, two canopies come closer to each other and then move farther away. This is a time dependent phenomenon. At time  $t = 03:36s$ , these two canopies start going in conical motion in counterclockwise direction about their vertical axis. This motion can be clearly seen in Figs. 4.5 (left and right). They rotate by about  $45^\circ$  in  $10:71s$ . Interestingly, this conical motion has also been observed in real life scenarios. I am not sure how the direction of rotation (clockwise or counter-clockwise) is chosen. I believe that a slight asymmetry in the mesh generated by the automatic mesh generator can give rise to counter-clockwise as being the preferred direction. In Figure 3: Cluster of two G-12 parachutes: Constructed (left) and prestressed (right) structural model. Figure 5 shows the pressure distribution on a plane cutting through the volume mesh and passing through the parachute canopy surfaces. As expected, there is a high pressure region inside of the canopy and lower pressure outside. This pressure gradient keeps the canopy inflated. In Figure 5(middle), a pair of vortices (the blue color spot signifies lower pressure at the core of a vortex) that are shed by the canopy can be seen in the downstream. These pairs of vortices shed from the left and right canopies are of different strengths implying that the aerodynamic responses of parachutes are not symmetric. Figure 5(right) shows a close view of the mesh viewed from the top and colored with pressure at  $t = 10:74s$ . Mesh is very  $\_ne$  close to the canopy surface. Whole simulations required 10 remeshes. Each remesh resulted in about 3 million elements and 0.5 million nodes. This implies that about 4 million unknown fluid variables were computed every nonlinear iteration in each time step. Total computational time required was about 200 hours using 32 processors on 16 nodes of a Linux cluster (2GB RAM/node, 1.7GHz P4 Xeon with 1.2GB/s Myrinet Switch).

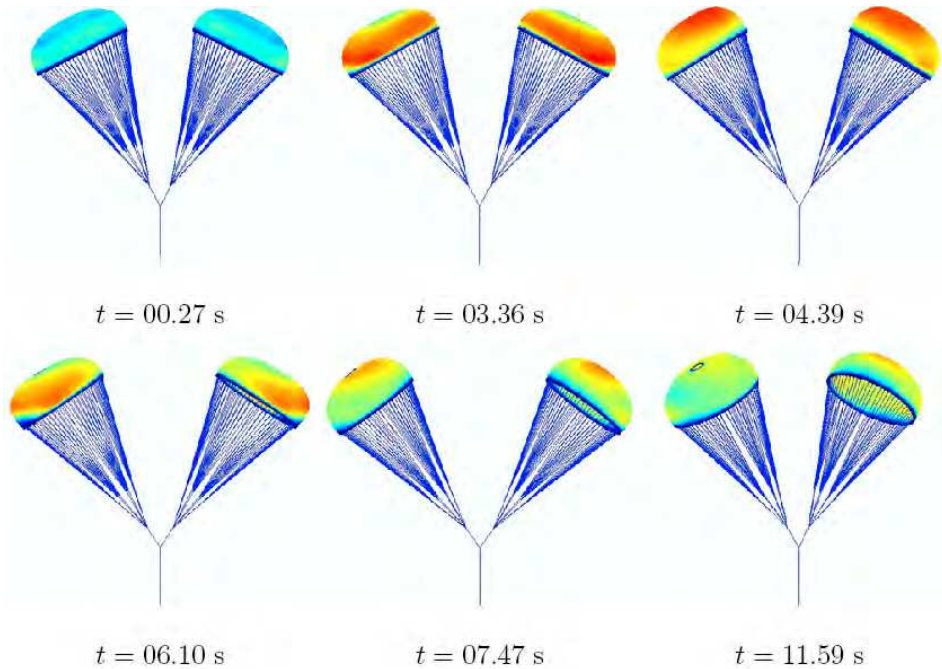


Fig. 4. G-12 parachute cluster with a fixed payload showing the deformed shapes and canopy pressure.

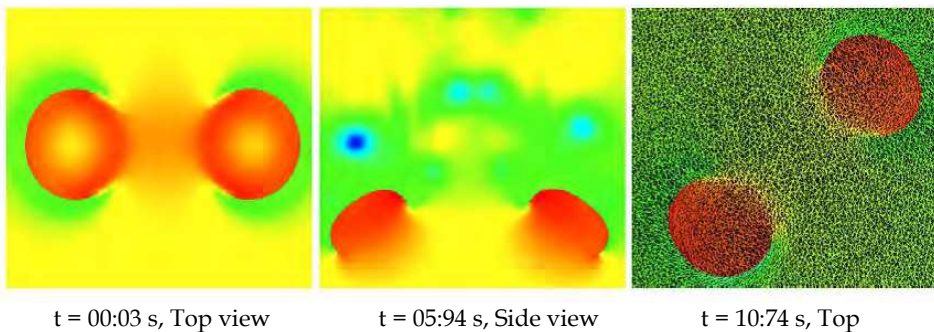


Fig. 5. G-12 parachute cluster with a fixed payload showing pressure (left and middle) and mesh colored with pressure (right) on a cross-section plane cutting through the parachutes.

#### Airdrop with free payload:

The pin was removed from the payload and the parachutes were released to fall with the payload weight. The total weight of the payload was 4,400 lb which is twice as heavy as that for a single parachute case. The flow results from a pinned case at  $t = 06:10s$ , when the FSI results were fully developed and free from startup conditions, were used as the initial conditions.

Figure 6 shows the shape of the parachutes and their fall in the vertical direction at three instants of time. In this figure, the fall position is determined with respect to an object falling with an assumed freestream velocity of 28 ft/s. The canopies are colored with pressure. With time they fall downward as expected implying that the terminal velocity in this case is higher than the assumed freestream velocity. Here, the cluster of parachutes with a payload of 4,400 lb is cruising at a terminal velocity of around 31 ft/s instead of 28 ft/s. Terminal velocity for a single parachute case is 28 ft/s. As expected, we lost the efficiency in cluster configuration. This implies that the impact velocity for the cluster at the time of landing would be higher than for a single parachute. This is not advisable for the safety of the payload. So, to find the terminal velocity of 28 ft/s in this case, we simulated a few more cases with lower payloads as shown in Figure 7. Following the trend of fall velocity for various payload weights from this figure, one notices that the lighter the payload, the lower the terminal velocity. One observes that the ideal weight for a payload would be about 3,600 lb. This weight will give a terminal velocity of 28 ft/s.

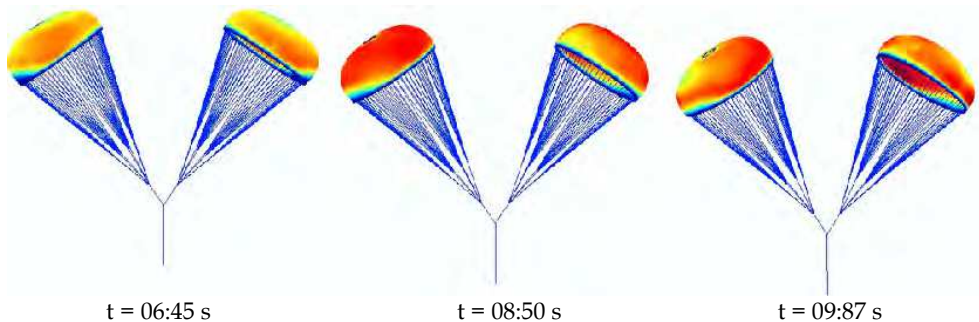


Fig. 6. Airdrop of payload using cluster of two G-12 parachutes: Parachute canopies colored with pressure.

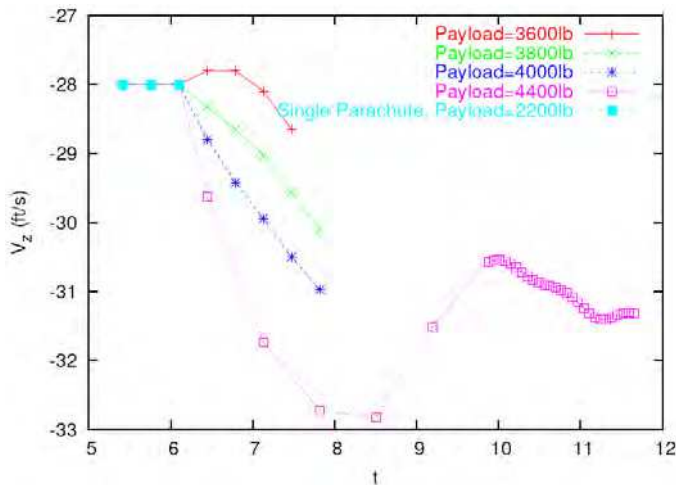


Fig. 7. Airdrop of a payload using a cluster of two G-12 parachutes: Fall velocity,  $V_z$  (ft/s) v/s time,  $t$  (s) for different weight of payload.

### Soft landing:

We carried out simulations of two G-12 cargo parachutes to study the soft landing behavior of such systems. *Soft landing* implies making the landing of paratroopers or cargos softer. Various techniques are used to achieve this. Pneumatic Muscle Actuator (PMA) is one technology to achieve this objective. In PMA, the risers are made of pneumatic muscles. When the cargo is very close to the ground the muscle is pressurized. The length of PMA starts contracting and in the process the canopies get pulled downward and the payload gets pulled upward reducing the impact velocity. Previous soft landing simulations focused on the soft landing for single T-10 personnel parachute and on comparisons with drop test data (Stein K. , Tezduyar, Sathe, Benney, & Charles, 2005). These simulations provide a level of confidence for simulations of soft landings with our computational methods. A follow-on simulation was carried out for a single G-12 cargo parachute with a 2,200 lb payload and a G-12 parachute weight of 130 lb (Stein K. , et al., 2003). In this example, soft landing is modeled by reducing the natural length of the retraction cable from 12.80 ft to 2.88 ft in 1 second.

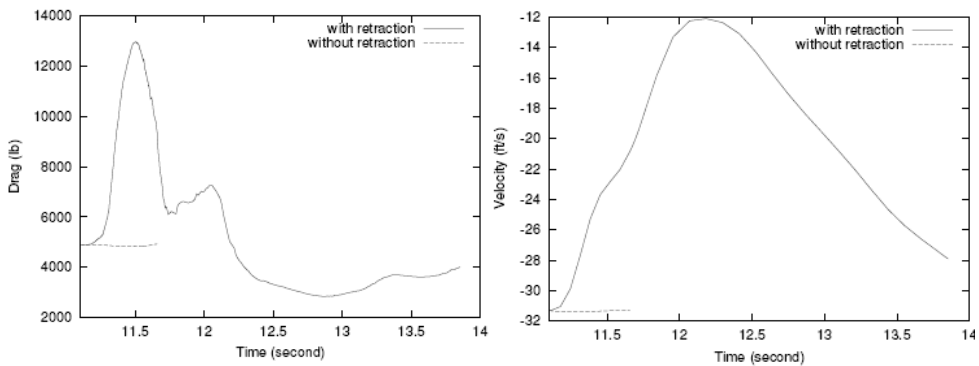


Fig. 8. Drag force (left) and payload velocity with a cluster of two G-12 parachutes during and after soft landing retraction.

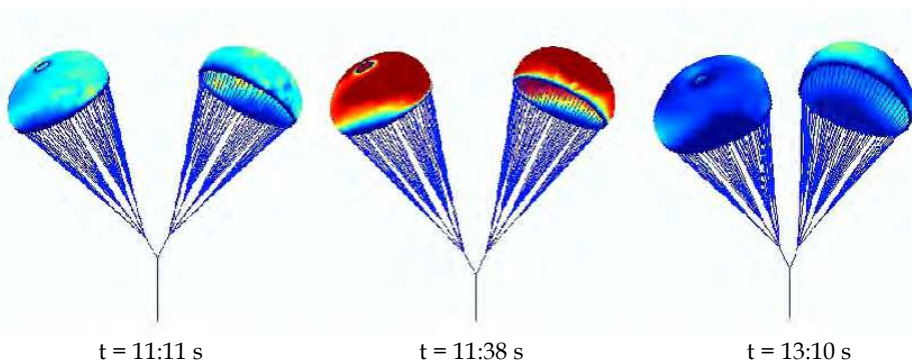


Fig. 9. G-12 parachute cluster at the start of pneumatic muscle contraction (left), at the end of contraction (middle) and after soft landing retraction showing the deformed shapes and canopy pressures.

While soft landing systems have been shown to be effective for single parachutes, little is known about the retraction process for a cluster of parachutes. In this simulation, the soft landing of a 4,400 lb cargo with a cluster of two G-12 parachutes is modeled to study the behavior during and after the retraction process. The soft landing computation is carried out after the parachute has reached a state of terminal descent. In this computation, a 26 ft retraction device is modeled with a cable that connects the confluence point of the two parachutes to the payload. Parachute-payload retraction is modeled by reducing the natural length of the retraction cable by 7.68 ft in 0.27 seconds. Finally, a series of computations are carried out with the retraction cable held at its reduced length after the retraction is completed to study the post retraction behavior of the G-12 cluster. In addition to the soft landing simulation, a second computation is carried out without soft landing retraction. This no-retraction case is a shorter computation and serves as a baseline for comparison with the soft landing case in Figure 8. The aerodynamic drag force on the G-12 cluster during and after soft landing retraction is shown in Fig. 4.8. The effect of the soft landing is apparent from the sharp increase in the drag force during retraction. It is important to note the dramatic drop in drag shortly after retraction ends. This drop is accompanied by canopy collapse and suggests that *harder* landings can be experienced if ground impact is delayed too long after retraction. The payload velocity during descent of the G-12 cluster with and without soft landing retraction is shown in Figure 8 (right). Decreased descent speed resulting from soft landing retraction is very evident, with the payload descent rate decreasing from 31.0 ft/s to 12.0 ft/s. A sequence of snapshots of the two G-12 parachutes during and after the soft landing, colored with the corresponding differential pressures on the canopy is shown in Figure 9. The first two snapshots (left and middle) correspond to times at the start of retraction and at the end of retraction. The final snapshot (right) corresponds to a time well after retraction has finished, with the canopies showing more severe parachute deformations. At the end, before the simulations are stopped, few gores collapsed resulting in gore-to-gore contact. Further FSI simulations are not possible without a contact model.

## 5.2 Cluster of three G-12 parachutes

Varying numbers of parachutes have been used in cluster configurations by the Army to test the efficiency of each configuration. The most commonly used configurations are clusters of two and three parachutes. A cluster of three parachutes is one of the simplest clusters of parachute configurations. One benefit of this configuration is that this configuration does not have the natural tendency of going in conical motion as observed for a two-parachute cluster. Stein et al. (Stein, et al., 2001; Stein K., et al., 2003)] presented the results from the stand-alone fluid dynamics simulations of a cluster of three rigid parachutes. The three parachute case presented more challenges in starting the FSI simulations than the two parachute case. Pressure ramping along with smaller time step was used to overcome the startup problems.

### Problem setup:

A fluid mesh is generated by joining three pieces (domain box, refinement box and parachutes). Several preparation stages similar to the one discussed for a cluster of the two parachute case in the previous section are required. Geometry modeler software package called GAMBIT (Fluent, 2001), was used to model the computational domain and parachute

geometry and to generate the surface meshes. The volume mesh is generated by an unstructured automatic mesh generator (Johnson A. , 1995; Johnson & Tezduyar, Mesh update strategies in parallel finite element computations of flow problems with moving boundaries and interfaces, 1994; Johnson & Tezduyar, Advanced mesh generation and update methods for 3D flow simulations, 1999). A refinement boundary is used to get a satisfactory level of mesh refinements near the canopy's boundary to capture the flow physics accurately. The automatic mesh generator creates about 6 million tetrahedral elements and 1 million nodes of fluid mesh, resulting in approximately 8 million unknowns per nonlinear iteration at each time step with DSD/SST formulations. The size of the structure mesh is negligible compared to the fluid mesh. The Reynolds number, based on radius of a flat G-12 parachute, is 5.5 million. We used the parallel FSI solver on 128 Cray T3E processors to arrive at the results. The freestream velocity, which corresponds to terminal velocity, is assumed to be 20 ft/s.

#### **Pinned payload:**

The computed results from the FSI simulations are shown in Figure 10. We notice that the symmetric distribution is lost as a result of the dynamic behavior of parachutes in this cluster configuration. The changes in pressure distribution on the canopies surfaces result in stronger parachute-to-parachute aerodynamic interactions. In fact, two of the parachutes came very close to each other at the end of simulations. The closer they got, the higher the frequency of remeshes were and the more difficult it became to perform FSI simulations. At the onset of contact, the simulations have to be terminated in the absence of a contact model.

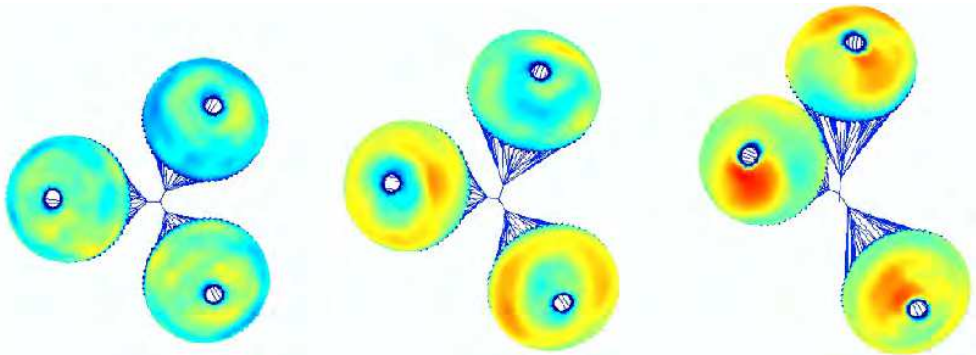


Fig. 10. Cluster of three G-12 parachutes at three different instances of time. Canopies are colored with pressure.

### **5.3 An example for compressible flow fluid-structure interaction simulation**

Our targeted goal is to study the behavior of parachute dynamic in compressible flow regime (i.e., flow with Mach number  $> 0.3$ ). Currently, the method has been tested for simple validation problems. Here, we present FSI results for a moving wedge problem in supersonic flow regime. The Mach number of the incoming fluid is 3.

At first, a solution for *fixed-wedge* case is arrived before switching moving algorithms. The *fixed-wedge* is used as the initial solution for the *moving-wedge*. The wedge is moving in the

downstream direction such that the equivalent freestream Mach number is 2.8. The computed values of Mach cone angles ( $\theta$ ) with the analytical values are compared. As observed in the table from Figure 11, there is a good agreement between these two results.

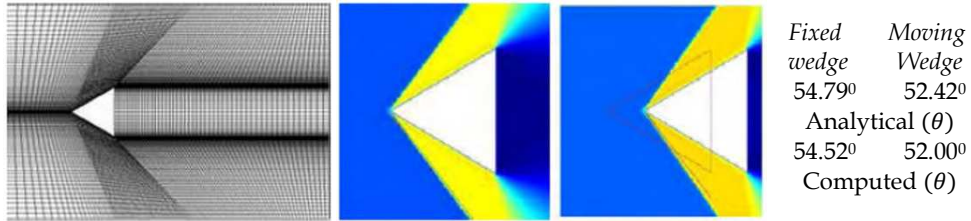


Fig. 11. Mesh with wedge (left), density at the beginning and end of the computations (center) and computed Mach cone angle ( $\theta$ ) compared for fixed and moving wedge with analytical solution.

## 6. Concluding remarks

In this chapter, we reviewed some computational challenges in fluid structure techniques. FSI simulations consisted of the following primary components: a solution method for the fluid dynamics, a solution method for the structural dynamics, an intelligent way to efficiently move and update a finite element mesh of fluid, and strategies for the coupling of fluid, and structural dynamics along the fluid-structure interface. The coupling is achieved in staggered fashion, with the fluid and structure coupled iteratively within a nonlinear iteration loop, and with multiple nonlinear iterations improving the convergence of the coupled system. The mesh domain was treated as a pseudo-elastic solid. To handle large structural-deformations, fluid dynamics solver required a methodology which can handle time-dependent spatial domain deformations. We presented Deforming-Spatial Domain / Stabilized Space-Time (DSD/SST) method which have a built-in capability to handle deforming structures. Semi-discrete formulations were used to carry out structural dynamics simulations which are based on the principle of virtual work. The SD model usually consists of membranes along with cables and payloads.

We presented results from the FSI simulations of a cluster of two G-12 parachutes under three for the parachute airdrop: fixed payload, airdrop, and soft-landing and cluster of three parachutes under fixed load conditions. Here, the parachute is represented as a structure composed of membranes, cables, and concentrated masses. The cables and membranes are assumed to have no flexural rigidity and experience large displacements and rotations. As a result, the interaction between a parachute system and the surrounding flow field is dominant in most of the parachute operations. Thus, the ability to predict parachute FSI is a challenge that must be faced in airdrop systems modeling. The G-12 parachute is a very large cargo parachute and its analysis presents convergence difficulties at the start of FSI simulations. A pressure ramping technique was proposed to deal with this start-up mismatch in the information exchange between the parachute's canopy and the fluid. It was found that a pressure ramping technique to smoothly transfer

the information between the fluid and structure solves the convergence problem encountered at the start of FSI simulations.

It was shown that one can ideally achieve an impact velocity as small as 12 ft/s using a soft-landing technique. However, for the 2-parachute cluster system, this minimum impact velocity is only achieved at a certain time after contraction. If one waits too long after contraction, the descent speed begins to increase, again, due to canopy collapse creating a harder landing. The amount of contraction is limited by the canopy strength because the loading on the canopy increases throughout the contraction process.

In a 3-parachute cluster system, we were able to predict that two parachutes collide as we observe in drop tests. We believe that this is caused by unsteady pressure distribution on the canopy surface as depicted in Figure 10. One can devise a control mechanism to prevent the collision of two canopies. One idea is to experiment with different control mechanisms such as heat-induced porosity-altering techniques for selected gores to introduce a sideways force.

The results from the FSI simulations of a cluster of three G-12 parachutes were also presented. The FSI simulations of both clusters of two and three parachute systems were found to suffer from contact issues. Two of the parachutes in this case came very close to contact. The FSI simulations faced a numerical barrier on the onset of contact. Similar contact issues were observed in the case of two parachute simulations when one or more gores collapsed. Further FSI simulations were not possible in the absence of a contact model.

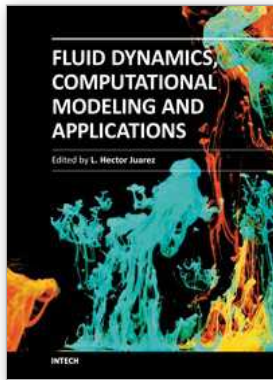
In future research, we need to improve the structural modeling capabilities for the cables, risers, and membranes by instantaneously addressing the non-isotropic and non-linear deformation of the flexible structures caused by changes in the fluid dynamics forces to imitate the physical reality. Additionally, the addition of a contact model will enable the formulations to continue after contact is made to simulate what happens physically when contact is made while the parachutes are still falling through the air. All such additions to the code will greatly increase the cost, so increased accuracy in the model simulations depends on computational resources and continued innovation in clock speeds and floating point operations per second (FLOPS). Another route of research to address the contact is to experiment with different control mechanisms to prevent contact.

## 7. References

- Babuska, I. (1973). The finite element method with Lagrange multipliers. *Numerische Mathematik*, 20, 179-192.
- Behr, M., & Tezduyar, T. (1994). Finite element solution strategies for large-scale flow simulations. *Computer Methods in Applied Mechanics and Engineering*, 112, 3-24.
- Brezzi, F. (1974). On the existence, uniqueness and approximation of saddle-point problems arising from Lagrangian multipliers. *Modelisation Math. Anal. Number*, 8, 129-151.
- Brooks, A., & Hughes, T. (1982). Streamline upwind/Petrov-Galerkin formulations for convection dominated flows with particular emphasis on the incompressible Navier-Stokes equations. *Computer Methods in Applied Mechanics and Engineering*, 32, 199-259.
- Butler, M. C. (2001). Additional applications of bat sombrero slider technology. *Proceedings of AIAA 16th Aerodynamic Decelerator Systems Technology Conference*.

- Fluent, I. (2001). *GAMBIT 2, CFD Preprocessor*. Lebanon, NH: Fluent, Inc.
- Hirsch, C. (1988). *Numerical Computation of Internal and External Flows: Fundamentals of Numerical Discretization* (Vol. 1). Chichester: John Wiley and Sons.
- Hughes, T. J., Franca, L. P., & Mallet, M. (1986). A new finite element formulation for computational fluid dynamics: I. symmetric forms of compressible Euler and Navier-Stokes equations and the second law of thermodynamics. *Computer Methods in Applied Mechanics and Engineering*, 54, 223-234.
- Johnson, A. (1995). Mesh Generation and Update Strategies for Parallel Computation of Flow Problems with Moving Boundaries and Interfaces. *Aerospace Engineering, University of Minnesota, Ph.D. thesis*.
- Johnson, A. A., & Tezduyar, T. E. (1994). Mesh update strategies in parallel finite element computations of flow problems with moving boundaries and interfaces. *Computer Methods in Applied Mechanics and Engineering*, 119, 73-94.
- Johnson, A. A., & Tezduyar, T. E. (1999). Advanced mesh generation and update methods for 3D flow simulations. *Computational Mechanics*, 23, 130-143.
- Kumar, V. (2005). *Advanced Computational Techniques for Incompressible / Compressible Fluid-Structure Interactions*. Rice University: Rice University.
- Le Beau, G., & Tezduyar, T. (1991). Finite element computation of compressible flows with the SUPG formulation. In *Advances in Finite Element Analysis in Fluid Dynamics* (Vols. FED-Vol-123, pp. 21-27). New York: ASME.
- Mittal, S. (1992). *Stabilized Space-Time Finite Element Formulations for Unsteady Incompressible Flows Involving Fluid-Body Interactions*. University of Minnesota.
- Sahu, J., & Benney, R. (1997). *Prediction of terminal decent characteristics of parachute clusters using CFD*. Technical report, AIAA Paper No. 97-1453.
- Shakib. (1988). *Finite Element Analysis of the Compressible Euler and Navier-Stokes Equations*. Ph.D. thesis, Stanford University, Mechanical Engineering.
- Stein, K. (1999). Simulation and Modeling Techniques for Parachute Fluid-Structure Interactions. *Aerospace Engineering, University of Minnesota, Ph.D. thesis*.
- Stein, K., Benney, R., Tezduyar, T., Kumar, V., Thornburg, E., Kyle, C., et al. (2001). Aerodynamic interaction between multiple parachute canopies. *Proceedings of the First MIT Conference on Computational Fluid and Solid*. Boston.
- Stein, K., Tezduyar, S., Sathe, S., Senga, M., Ozcan, C., Soltys, T., et al. (2003). Simulation of parachute dynamics during control line input operations. *Proceedings of the 17th AIAA Aerodynamic Decelerator Systems Technology Conference*. Monterey, California.
- Stein, K., Tezduyar, T. E., Sathe, S., Benney, R., & Charles, R. (2005). Fluid-structure interaction modelling of parachute soft-landing dynamics. *International Journal for Numerical Methods in Fluids*, 47, 619-631.
- Stein, K., Tezduyar, T., Kumar, V., Sathe, S., Benney, R., Thornburg, E., et al. (2003). Aerodynamic interactions between parachute canopies. *Journal of Applied Mechanics*, 70, 50-57.
- Tezduyar, T. E. (1992). Stabilized finite element formulations for incompressible flow computations. *Advances in Applied Mechanics*, 1-44.
- Tezduyar, T. E., Behr, M., & Liou, J. (1992). A new strategy for finite element computations involving moving boundaries and interfaces - the deforming-spatial-domain/space time procedure: I. the concept and the preliminary tests. *Computer Methods in Applied Mechanics and Engineering*, 339-351.

- Tezduyar, T., Mittal, S., Ray, S., & Shih, R. (1992). Incompressible flow computations with stabilized bilinear and linear equal-order-interpolation velocity pressure. *Computer Methods in Applied Mechanics and Engineering*, 95, 221-242.
- Udoewa, V. (2005). *Computational Techniques for Aerodynamic Interactions between*. Rice University: Mechanical Engineering and Material Science.



## **Fluid Dynamics, Computational Modeling and Applications**

Edited by Dr. L. Hector Juarez

ISBN 978-953-51-0052-2

Hard cover, 660 pages

**Publisher** InTech

**Published online** 24, February, 2012

**Published in print edition** February, 2012

The content of this book covers several up-to-date topics in fluid dynamics, computational modeling and its applications, and it is intended to serve as a general reference for scientists, engineers, and graduate students. The book is comprised of 30 chapters divided into 5 parts, which include: winds, building and risk prevention; multiphase flow, structures and gases; heat transfer, combustion and energy; medical and biomechanical applications; and other important themes. This book also provides a comprehensive overview of computational fluid dynamics and applications, without excluding experimental and theoretical aspects.

### **How to reference**

In order to correctly reference this scholarly work, feel free to copy and paste the following:

Vinod Kumar and Victor Udoewa (2012). Fluid-Structure Interaction Techniques for Parachute, Fluid Dynamics, Computational Modeling and Applications, Dr. L. Hector Juarez (Ed.), ISBN: 978-953-51-0052-2, InTech, Available from: <http://www.intechopen.com/books/fluid-dynamics-computational-modeling-and-applications/fluid-structure-interaction-techniques-for-parachute>

# **INTECH**

open science | open minds

### **InTech Europe**

University Campus STeP Ri  
Slavka Krautzeka 83/A  
51000 Rijeka, Croatia  
Phone: +385 (51) 770 447  
Fax: +385 (51) 686 166  
[www.intechopen.com](http://www.intechopen.com)

### **InTech China**

Unit 405, Office Block, Hotel Equatorial Shanghai  
No.65, Yan An Road (West), Shanghai, 200040, China  
中国上海市延安西路65号上海国际贵都大饭店办公楼405单元  
Phone: +86-21-62489820  
Fax: +86-21-62489821

© 2012 The Author(s). Licensee IntechOpen. This is an open access article distributed under the terms of the [Creative Commons Attribution 3.0 License](#), which permits unrestricted use, distribution, and reproduction in any medium, provided the original work is properly cited.